Journal of Materials Chemistry A

ROYAL SOCIETY OF CHEMISTRY

PAPER

View Article Online
View Journal | View Issue

Cite this: J. Mater. Chem. A, 2025, 13, 27661

Interlayer-stacking mode modulation in an imine covalent organic framework for efficient photocatalytic hydrogen production†

Kang-Hua Li,[ab] Li-Na Liu,[c] Zhong-Xin Xue,[a] Zi-Wen Xu,[a] Yogesh Gawale,[a] Fu-Gang Zhao*[d] and Wei-Shi Li *[abc]

Two-dimensional conjugated covalent organic frameworks (COFs) have emerged as a new class of promising photocatalysts for solar-hydrogen energy conversion. The regulation of their interlayer stacking mode is an important strategy to modulate their properties and photocatalytic performance. Historically, the staggered AB mode has seldom demonstrated greater photoactivity than the corresponding eclipsed AA mode. Herein, a contrary example is presented, wherein the AB-stacked **PyDBTSO-AB** COF outperforms its AA-stacked isomer, **PyDBTSO-AA** COF. This pair of isostructured COFs was synthesized from the same tetraaniline-functionalized pyrene (Py) monomer and dibenzaldehyde-functionalized dibenzothiophene sulfone (DBTSO) monomer under conventional solvothermal conditions in an *o*-dichlorobenzene/butanol/acetic acid-mixed medium and under ionothermal conditions in 1-butyl-3-methylimidazolium tetrafluoroborate ionic liquid, respectively. Structural characterizations revealed that **PyDBTSO-AA** possesses a larger specific surface area and void pore volume, whereas **PyDBTSO-AB** exhibits greater hydrophilicity and a shorter interlayer π–π stacking distance. Furthermore, electrochemical impedance spectroscopy and photocurrent responsive experiments revealed that **PyDBTSO-AB** has a smaller charge transport impedance and a larger photocurrent responsiveness than **PyDBTSO-AA**. Finally, in photocatalytic hydrogen production experiments conducted with Pt co-catalyst under full-arc Xe light irradiation, **PyDBTSO-AB** achieved a hydrogen evolution rate of 109.6 mmol g^{-1} h^{-1}, more than twice that displayed by **PyDBTSO-AA**. Consequently, this research emphasizes the equal importance of the AB-stacking mode in comparison to the AA-stacking mode within the realm of photocatalytic COF design and provides new insights into the manner in which their interlayer-stacking modes influence the ultimate photocatalytic activities.

Received 18th February 2025
Accepted 14th July 2025

DOI: 10.1039/d5ta01336d

rsc.li/materials-a

Introduction

In order to address the challenges pertaining to the sustainability of human society, such as the exponential surge in energy demand, the rapid escalation of environmental pollution, and global climate change, it is imperative to develop a reliable technology capable of consistently providing green and renewable energy as an alternative to conventional fossil fuels.[1–4] As one of the potential solutions, solar hydrogen production technology, which utilizes solar power to produce hydrogen from water and converts solar energy into reusable chemical energy, has been extensively studied since 1972.[5] To date, a variety of photocatalysts including inorganic and organic semiconductors have been designed and investigated;[6–19] however, the state-of-the-art solar-to-hydrogen conversion (STH) efficiency remains lower than 2%, which is significantly lower than the basic requirement (10% as predicted[20]) for its practical use. Therefore, the exploration of efficient photocatalysts remains a core challenge in the field.

Featuring a two- or three-dimensionally extended rigid framework, periodically built-in pores, and high crystallinity, covalent organic frameworks (COFs) have been widely recognized as one of the ideal platforms for designing organic photocatalysts for solar hydrogen production with high performance.[21,22] The pioneering work dates back to 2010, when Müllen, Wang, and coworkers reported the use of A_3B_2-type poly(azomethine) polymers (imine-based COFs) as

[a]State Key Laboratory of Fluorine and Nitrogen Chemistry and Advanced Materials, Shanghai Institute of Organic Chemistry, University of Chinese Academy of Sciences, Chinese Academy of Sciences, 345 Lingling Road, Shanghai 200032, P. R. China. E-mail: liws@mail.sioc.ac.cn

[b]The Education Ministry Key Laboratory of Resource Chemistry, Shanghai Normal University, Shanghai 200234, P. R. China

[c]Engineering Research Center of Zhengzhou for High Performance Organic Functional Materials, Zhengzhou University of Technology, 6 Yingcai Street, Huiji District, Zhengzhou 450044, P. R. China

[d]School of Chemistry and Chemical Engineering, Zhejiang Sci-Tech University, Hangzhou 310018, China. E-mail: fgzhao@zstu.edu.cn

† Electronic supplementary information (ESI) available. See DOI: https://doi.org/10.1039/d5ta01336d

photocatalysts.[23] Later, in 2014, Lotsch *et al.* found that hydrazone-linked triazine COFs can deliver a photocatalytic hydrogen evolution rate (HER) of 1.97 mmol g^{-1} h^{-1}.[24] Since then, a huge number of COFs with large structural diversity have been designed and studied, and significant progress in photocatalytic performance has been achieved. For example, Cooper *et al.* utilized benzobis(benzothiophene sulfone) as a key building block in the synthesis of a β-ketoenamine-linked COF and reported a visible-light-photocatalytic HER of 16.3 mmol g^{-1} h^{-1}.[25] In 2022, a vinylene-linked donor–acceptor (D–A) fully conjugated COF named BTH-3, bearing electron-deficient benzobisthiazole and electron-rich benzotrithiophene as A and D units, respectively, demonstrated a HER of 15.1 mmol g^{-1} h^{-1} under visible light irradiation.[26] One year later, a similar vinylene-linked fully conjugated COF named COF-JLU35, composed of benzotrithiophene donor and triazine acceptor units, demonstrated a significantly higher HER of 70.8 mmol g^{-1} h^{-1} under visible light irradiation.[27] The record HER value was enhanced to 288.8 mmol g^{-1} h^{-1} by a zwitterionic vinylene-linked COF named ZV-COF-1 in the same year[28] and now further updated to 390.68 mmol g^{-1} h^{-1} by hybridizing a COF with a hydrogen-bonded organic framework (HOF) to form an S-scheme heterojunction.[29]

Clearly, the selection and innovation of building blocks as well as their linkages are of primary importance in the design of COF materials. This is because they fundamentally determine chemical composition, framework structure, and the expected properties and functions of the target COF. Therefore, it is common to see the adoption of a D–A structure in COF photocatalysts[30–34] since such a structure can bring many benefits for photocatalysis, including narrowing bandgap, expanding light-absorption spectrum, promoting exciton dissociation and charge separation, strengthening interchain interactions and packing, facilitating charge transport.

Besides the composition, the layer-stacking mode is another important factor that governs many intrinsic properties of COF materials, including porosity, crystallinity, interlayer charge separation, and transport. In a two-dimensional (2D) COF with a fixed framework, interlayer stacking can adopt either an eclipsed AA mode or a staggered mode, such as AB or ABC. Only AA-stacking enables all the pores in the framework to form one-dimensional channels with the same large diameters, which enables the COF scaffolds, even those are buried deeply inside their bulk, to maintain good accessibility and mass exchange to the outer medium and species. If the D–A structure is adopted in the framework, AA-stacking can produce segregated D and A self-packing columns. This can provide new charge transport pathways in addition to the framework for the separated hole and electron charge carriers to migrate away from each other and thus reduce their recombination risk. Therefore, AA-stacking is generally thought to be more favorable for heterogeneous photocatalysis than any of the staggered modes. However, this has not been fully demonstrated to date. This is because in most reported works, only the AA-stacking scenario has been investigated. In a few recent works, COFs with different stacking modes have been synthesized and compared. For example, Seki *et al.* synthesized several pairs of β-ketoenamine-linked COF isomers adopting either AA- or AB-stacking mode under solvothermal conditions with different temperatures, and found the AA-stacking COFs display better photocatalytic performance than the corresponding AB-stacking ones, with up to 8-fold improvements.[35] In another work, benzothiadiazole-based β-ketoenamine-linked COF isomers were found to show different preferences in the photosensitized generation of type I and type II reactive oxygen species, in which the AA-stacking prefers the latter while the ABC-stacking tends to produce the former.[36] More recently, two imine-linked COFs bearing copper cyclic trinuclear units as nodes were reported to reversibly change their stacking mode between AA and ABC modes upon heat treatment in different solvent media, in which the AA-stacking framework displayed broader light absorption spectra, more efficient charge separation, and higher photocatalytic O_2-sensing performance.[37] In another trinuclear copper organic framework system, AA- and ABC-stacking isostructures can be prepared in the presence of different organic acids in the reaction media.[38] Still, the AA-stacking proved to be more efficient than the ABC-stacking in photocatalytic reduction of U(VI) for removing radioactive pollution. Although these examples show that AA-stacking facilitates photocatalysis in most cases, the number of related reports is limited and thus cannot fully reveal the impact of the interlayer stacking mode on photocatalytic performance.

Herein, we report an example of an imine-linked AB-stacking COF named **PyDBTSO-AB** that has better photocatalytic hydrogen production performance than its AA-stacked isomer **PyDBTSO-AA** (Fig. 1a). The COFs adopted dibenzothiophene sulfone (DBTSO) as a linear arm and acceptor moiety, while pyrene (Py) was used as a branching node unit and electron-donating moiety in the scaffold. DBTSO is a very common building block for the design of hydrogen production photocatalysts since it can serve as a photocatalytic reactive center in addition to acting in its acceptor role in the D–A structure, and has demonstrated good performance in most reported works.[39–43] In this study, the different interlayer stacking isomers were obtained by changing solvothermal conditions, in which the conventional conditions using 1,2-dichlorobenzene (*o*DCB) and *n*-butanol (BuOH)-mixed solvent as reaction media and together with acetic acid (AcOH) as a catalyst afforded an AA-stacking product (**PyDBTSO-AA**), while the conditions using 1-butyl-3-methylimidazolium tetrafluoroborate ($[C_4mim][BF_4]$) ionic liquid as reaction medium gave the AB-stacking product (**PyDBTSO-AB**). It was found that the former displayed significantly larger Brunauer–Emmett–Teller (BET) specific surface area (SSA) and void space, but the latter inversely exhibited more intense π–π interlayer interactions and efficient charge separation and transportation. Intriguingly, the AB-stacking COF **PyDBTSO-AB** finally outperformed the AA-stacking **PyDBTSO-AA**, and delivered a HER of 109.6 mmol g^{-1} h^{-1} under full-arc Xe lamp irradiation. This is more than twice that of **PyDBTSO-AA** and marks **PyDBTSO-AB** as one of the highly efficient COF photocatalysts in the field.

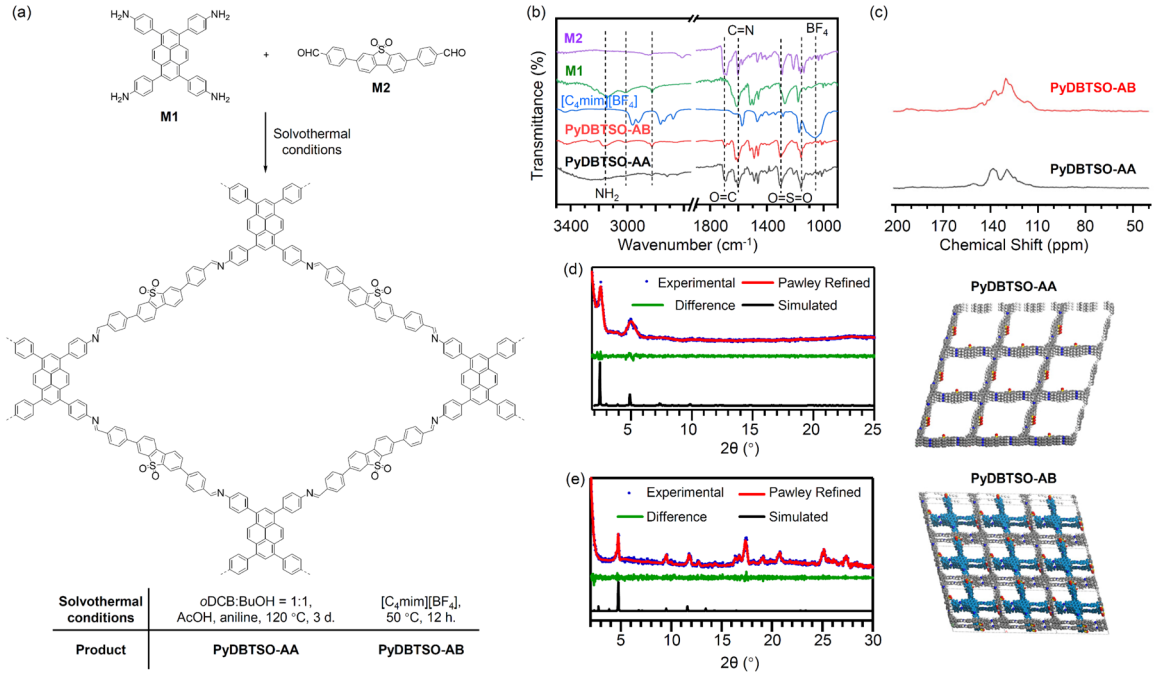

Fig. 1 (a) Synthetic route and conditions for **PyDBTSO-AA** and **PyDBTSO-AB**. (b) FT-IR spectra of **M1**, **M2**, $[C_4mim][BF_4]$ ionic liquid, **PyDBTSO-AA** and **PyDBTSO-AB**. (c) Solid-state ^{13}C NMR of **PyDBTSO-AA** and **PyDBTSO-AB**. (d and e) Experimental, Pawley refined, and simulated PXRD patterns and space-filling models of the crystalline structures of (d) **PyDBTSO-AA** and (e) **PyDBTSO-AB**.

Experimental section

Chemicals and materials

Unless otherwise stated, all reagents were obtained from commercial sources and used as received. 4,4′,4″,4‴-(Pyrene-1,3,6,8-tetrayl)tetraaniline (**M1**) was purchased from Macklin Company and Dyotechlife Pvt Ltd. According to the reported methods,[44,45] 3,7-dibromo dibenzo[*b*,*d*]thiophene-5,5-dioxide was synthesized, then submitted to Suzuki coupling with 4-formylbenzeneboronic acid pinacol ester to afford 4,4′-(5,5-dioxidodibenzo[*b*,*d*]thiophene-3,7-diyl) dibenzaldehyde (**M2**). Experimental details of the synthesis of **M2** are provided in the ESI.† Its chemical structure was unambiguously characterized and identified by ^1H NMR spectroscopy (Fig. S1†) and mass spectrometry (Fig. S2†).

Synthesis of covalent organic frameworks

PyDBTSO-AA. Into a 10 mL Pyrex tube, **M1** (28.34 mg, 0.05 mmol), **M2** (42.4 mg, 0.1 mmol), aniline (72.9 μL, 0.8 mmol), 0.4 mL AcOH, 2 mL *o*DCB and 2 mL BuOH were added to form the reaction mixture. The reaction mixture was sonicated for 10 min and degassed through three freeze–pump–thaw cycles. The Pyrex tube was then sealed under vacuum and heated at 120 °C for 3 days. After cooling to room temperature, the mixture was filtered to separate the precipitated crude product. The crude product was purified by repeated washing with water, dichloromethane, and tetrahydrofuran, and subsequently dried under vacuum at 120 °C for 8 h. The process yielded 63.97 mg of pure **PyDBTSO-AA** as a yellow solid powder, corresponding to a yield of 90%.

PyDBTSO-AB. In a 25 mL round-bottomed flask, **M1** (14.17 mg, 0.025 mmol), **M2** (21.2 mg, 0.05 mmol), and 200 μL $[C_4mim][BF_4]$ ionic liquid were added and the mixture was stirred vigorously at 50 °C for 12 h. Subsequently, the reaction mixture was poured into ethanol to precipitate the product. After filtration, the obtained crude product was washed three times with ethanol and acetone to remove residual ionic liquid, unreacted monomers, and low molecular weight oligomers. The resulting product was then dried in a vacuum oven, affording 25.6 mg **PyDBTSO-AB** as a yellow solid powder corresponding to a yield of 72%.

Results and discussion

As shown in Fig. 1a, the two iso-structured COFs with different interlayer stacking modes, **PyDBTSO-AA** and **PyDBTSO-AB**, were synthesized by imine-formation polycondensation between a tetraaniline-functionalized Py monomer, **M1**, and a dibenzaldehyde-functionalized DBTSO monomer, **M2**, under different solvothermal conditions. Under conventional solvothermal conditions using *o*DCB/BuOH (v/v: 1/1) as solvent and AcOH as acid catalyst, the polycondensation afforded **PyDBTSO-AA** COF bearing an AA-stacking mode in a yield of 90%. In the reaction, 8 equivalents of aniline were used as a competitive monomer to slow down the reaction to establish better crystallinity in the product. When the reaction was conducted with $[C_4mim][BF_4]$ ionic liquid as a solvent, the AB-stacking **PyDBTSO-AB** COF was finally produced in a yield of 72%. In contrast to the conventional solvothermal conditions, the reaction in ionic liquid solvent did not require an acid catalyst, and the reaction temperature could be lowered to 50 °C.

Table 1 Structural characterizations, basic properties and photocatalytic performances of PyDBTSO-AA and PyDBTSO-AB COFs

	Elemental analysis[a] (%)			Porosity							
COF	C	H	N	SSA ($m^2\ g^{-1}$)	P_{avg} (nm)	V_{total} ($cm^3\ g^{-1}$)	E_g (eV)	τ_{avg} (ns)	CB (eV)	VB (eV)	HER (mmol $g^{-1}\ h^{-1}$)
PyDBTSO-AA	79.73	4.29	3.92	338	2.7	0.41	2.15	1.01	−0.84	1.31	46.8
PyDBTSO-AB	75.95	4.23	3.06	20	1.7	0.06	2.19	1.00	−0.73	1.46	109.6

[a] Theoretically calculated: C 80.60%, H 5.61%, N 2.47%.

The chemical structures of the two obtained COFs were characterized and identified by elemental analysis, Fourier transform infrared (FT-IR), and solid-state ^{13}C nuclear magnetic resonance (^{13}C ssNMR) spectroscopies. As shown in Table 1, the deviations of C, H, and N contents between their experimental and theoretical values were found to be within the general levels for a polymer product[46–48] in both **PyDBTSO-AA** and **PyDBTSO-AB**, confirming the correctness in their chemical compositions. In FT-IR (Fig. 1b), two strong characteristic N–H stretching vibration peaks for primary amino units were observed at 3458 and 3364 cm^{-1} in the spectrum of the starting monomer **M1**.[49–53] In the spectrum of the second starting monomer **M2**, the stretching vibration peak of aldehyde units was identified at 1698 cm^{-1}. These peaks were found to dramatically attenuate in the COF products, **PyDBTSO-AA** and **PyDBTSO-AB**. In place, the characteristic stretching vibration peak from the formed C=N bonds newly appeared at 1607 cm^{-1}, providing solid evidence for the smooth occurrence of the polycondensation reaction. However, it is noticeable that the above IR peaks of the primary amino and aldehyde units did not completely vanish; a certain amount remained in the final COF products. Judging from their intensities, **PyDBTSO-AA** seems to possess larger numbers of residual aldehyde units, but fewer residual primary amino units as compared to **PyDBTSO-AB**. This implies that the different reaction conditions tend to keep different edge functionalities in the growing frameworks. Besides these, **PyDBTSO-AA** and **PyDBTSO-AB** displayed both characteristic IR peaks from the Py unit at 1515, 1494, and 1459 cm^{-1} and from the DBTSO units at 1307 and 1157 cm^{-1}, confirming the successful integration of Py and DBTSO in their scaffolds. Moreover, as compared to that of [C_4mim][BF_4], the IR spectrum of **PyDBTSO-AB** was found to have no peaks associated with ionic liquid molecules, such as C–H stretching vibration peaks of imidazole ring at 3162 and 3121 cm^{-1}, C–H stretching peaks of methyl and butyl side chains at 2964 and 2937 cm^{-1}, and BF_4^- peak at 1036 cm^{-1}. This indicates that almost no [C_4mim][BF_4] remained in the final **PyDBTSO-AB** product. In the ^{13}C NMR spectra shown in Fig. 1c, a peak at 150.87 ppm was observed in both **PyDBTSO-AA** and **PyDBTSO-AB** spectra. This peak can be assigned to the carbon in the C=N imine bond, confirming again its generation in the reaction. Furthermore, the signals from the carbon adjacent to the sulfone functionality in the DBTSO units and those from electron-rich pyrene units in both COF spectra were observed at 138 and 129–118 ppm, respectively, illustrating again the successful integration of Py and DBTSO units in both COF scaffolds.

The crystalline and interlayer-packing modes of the synthesized COFs were investigated by powder X-ray diffraction (PXRD) and theoretical structural simulation with Materials Studio software. As shown in Fig. 1d, the **PyDBTSO-AA** powder exhibited two intense X-ray diffraction peaks at 2θ values of 2.50° and 5.03°, indicating its crystalline nature. Structural construction by the Forcite module and Pawley refinement by the Reflex module in Materials Studio predict that **PyDBTSO-AA** COF adopts a 3D triclinic crystal lattice with an AA-stacking mode. The lattice parameters are $a = 36.4$ Å, $b = 36.3$ Å, $c = 4.56$ Å, $\alpha = \beta = 90°$ and $\gamma = 72.0°$, while the Pawley refinement parameters are $R_p = 6.11\%$ and $R_{wp} = 7.88\%$. In the case of **PyDBTSO-AB** COF, the PXRD profile (Fig. 1e) displayed a couple of diffraction peaks in the 2θ range of 4°–30°, with the first appearing at 4.79°. Structural simulation and XRD refinement suggest a 3D triclinic lattice bearing the unit parameters of $a = 39.3$ Å, $b = 39.1$ Å, $c = 7.79$ Å, $\alpha = \beta = 90°$, $\gamma = 108.1°$ and an AB-interlayer stacking mode. The refinement parameters are $R_p = 6.86\%$ and $R_{wp} = 8.83\%$. These results confirm that the variation in solvothermal conditions for imine-formation polycondensation afforded different interlayer-stacking modes for the produced COF isomers, which would have a great impact on their basic properties and photocatalytic performance. Notably, in addition to different interlayer-packing modes, PXRD profiles also reveal another important structural discrepancy between the two COFs. That is, **PyDBTSO-AB** displayed two sharp X-ray diffraction peaks at 2θ values of 25.1° and 27.4°, whereas no peaks were observed in the same region in the **PyDBTSO-AA** profile. This illustrates that the strong interlayer π–π stacking only exists in **PyDBTSO-AB** COF and not in **PyDBTSO-AA** COF, which would be another important factor that influences their photocatalytic performance.

The morphology and microstructural details of the COFs were investigated by scanning electron microscopy (SEM) and transmission electron microscopy (TEM). As can be seen from Fig. 2a, b, e, and f, both COFs appeared to be formed as particles with a piled sheet morphology. In the TEM images shown in Fig. 2c and g, such piled sheet structures were further confirmed. Moreover, from the high-resolution TEM images displayed in Fig. 2d and h, the embedded pore structures in both COF sheets can be clearly seen, and the pore size of **PyDBTSO-AA** was found to be larger than that of **PyDBTSO-AB**. In nitrogen adsorption and desorption experiments (Fig. 2i and j), both **PyDBTSO-AA** and **PyDBTSO-AB** COFs exhibited a type-IV isothermal behavior. Based on BET theory, the SSAs of **PyDBTSO-AA** and **PyDBTSO-AB** COFs were calculated to be 338

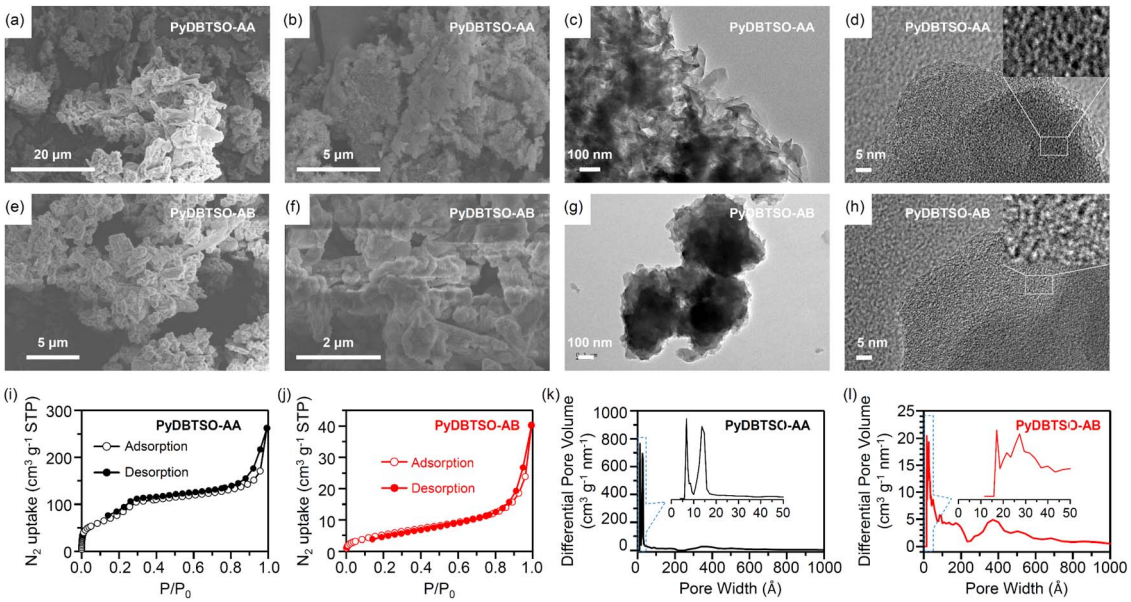

Fig. 2 (a, b, e and f) SEM, (c, d, g and h) TEM, (i and j) N_2-adsorption and desorption isotherms and (k and l) pore size distribution profiles of **PyDBTSO-AA** and **PyDBTSO-AB** COFs.

and 20 $m^2 g^{-1}$ (Table 1). Clearly, **PyDBTSO-AA** has a much larger SSA than **PyDBTSO-AB**. The pore size distributions were estimated using nonlocal density functional theory (NLDFT). As shown in Fig. 2k and l, **PyDBTSO-AA** exhibited two peaks at 13.6 and 27.3 Å, while **PyDBTSO-AB** displayed a relatively broad distribution in the range of 15–800 Å. This can be well explained by considering that the eclipsed AA-stacking allows all the embedded pores in each 2D framework to form one-dimensional channels by respectively piling themselves up one by one. In contrast, the pores are partially blocked by the skeletons of neighboring layers in the staggered AB-stacking and thus cannot form the uniform, straight-line-like channels. In general, this will decrease the accessibility of inner surfaces toward outside species and thus disfavor photocatalysis.

Light absorption and exciton generation are two important initial steps in a photocatalysis reaction. In this work, we used ultraviolet-visible (UV-vis) diffuse reflectance spectroscopy (DRS), photoluminescence (PL) spectroscopy, and time-correlated single-photon-counting (TCSPC) fluorescence decay spectroscopy to assess the behaviors of the two studied COFs in these two processes. As revealed in Fig. 3a, both **PyDBTSO-AA** and **PyDBTSO-AB** COFs exhibited strong and similar light absorption in the spectral range from 300–800 nm, covering from UV to visible and to the near-infrared (NIR) region. By constructing Tauc plots (Fig. S4†), their optical band gaps were evaluated to be 2.15 and 2.19 eV, respectively (Table 1). Upon excitation at 440 nm, the reference compounds, **Py-imine** (ref. 54) and **DBTSO-imine** (see the ESI† for details of the synthesis and ^{1}H NMR spectrum) that represent imine-furnished Py and DBTSO building blocks in the COFs, respectively, displayed intense fluorescence in the region of 450–600 nm (Fig. 3b). In comparison, both **PyDBTSO-AA** and **PyDBTSO-AB** COFs exhibited very weak fluorescence. The observed fluorescence quench phenomena indicate that the combination of Py and DBTSO in the COF scaffold forms an effective D–A structure that enables photogenerated excitons to quickly dissociate into free charge carriers *via* efficient intramolecular photoinduced electron transfer from D to A components. By using the TCSPC technique, the fluorescence decay profiles of the two COFs were acquired by monitoring at 420 nm (Fig. 3c) and then deconvoluted into the two components shown in Table S1.† Although these components differed in lifetime and amplitude, the average lifetimes calculated for the two COFs gave similar values; *i.e.*, 1.01 ns for **PyDBTSO-AA** and 1.00 ns for **PyDBTSO-AB**. From these analyses, we deduce that the different interlayer packing modes in **PyDBTSO-AA** and **PyDBTSO-AB** do not have a significant influence on the material light absorption, exciton generation, or exciton dissociation processes.

For an efficient photocatalyst, proper alignment of its electronic band structure is a primary prerequisite. Here, electrochemical Mott–Schottky (M–S) plots were used to determine the flat bands (FBs) of the two studied COFs and then calculate their band structures together with optical bandgaps. As shown in Fig. S5,† both COFs displayed M–S curves with positive slopes, indicating they are n-type semiconductors and have a conduction band (CB) potential equal to FB potential.[55] Thus, based on the assessed FB potentials (−1.04 and −0.93 V *vs.* Ag/Ag^+) by M–S plots, the CBs of **PyDBTSO-AA** and **PyDBTSO-AB** were calculated to be −3.66 and −3.77 eV, respectively (Fig. 3d). Subsequently, from their CB and optical bandgap data, the valence bands (VBs) were derived to be −5.81 eV for **PyDBTSO-AA** and −5.96 eV for **PyDBTSO-AB**. Clearly, as compared to the AA-stacking mode, the AB-stacking adopted by the COF lowers the CB and VB energy levels significantly, which would impact their photocatalytic performances.

Moreover, electrochemical impedance spectroscopy (EIS) and photocurrent responsive experiments were carried out to investigate charge transport and photo-triggered charge carrier

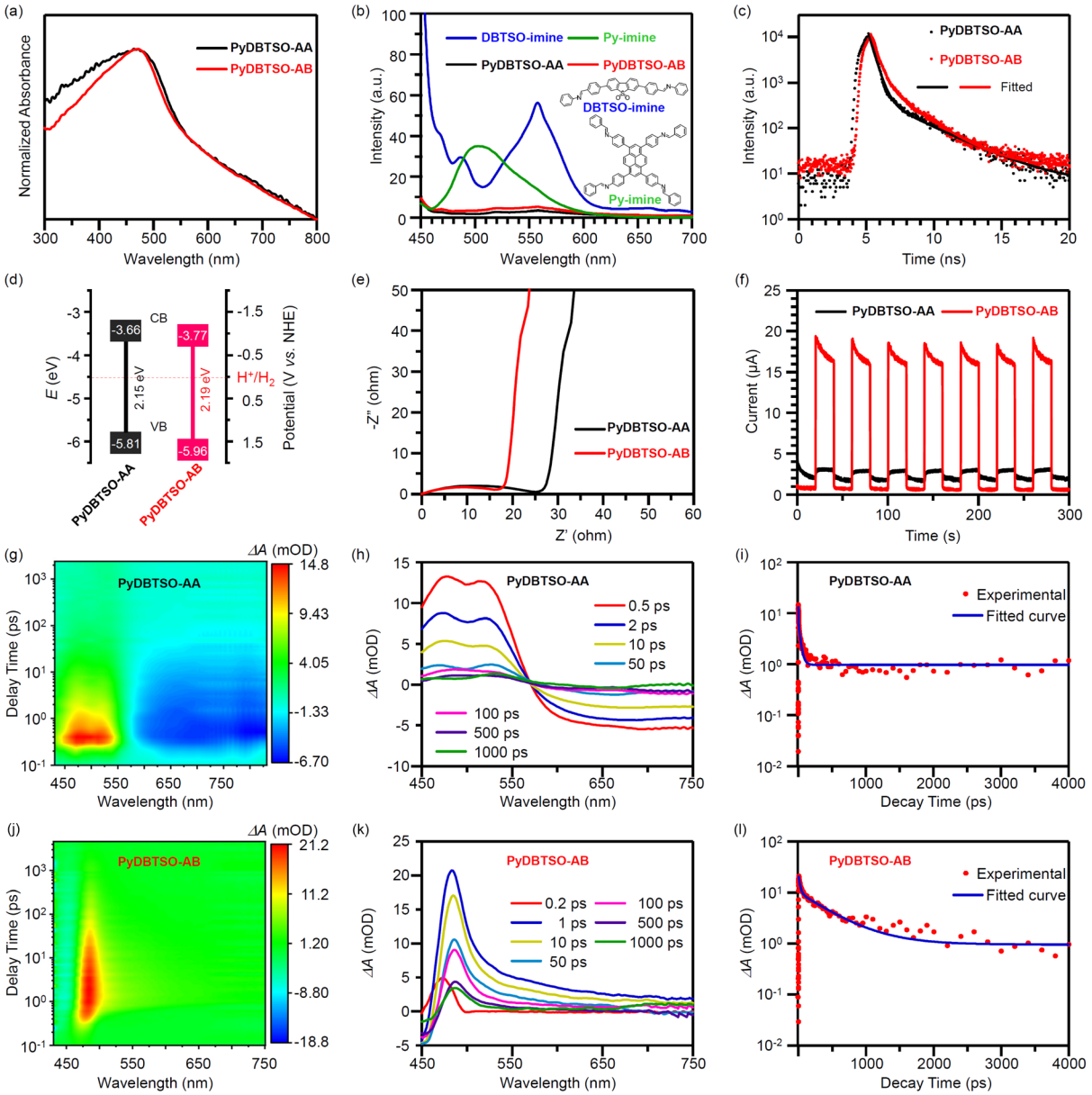

Fig. 3 (a) UV-vis diffuse reflectance spectra, (b) photoluminescent spectra upon excitation at 440 nm, (c) fluorescent decay profiles monitored at 420 nm, (d) energy level band diagrams, (e) electrochemical impedance spectra, and (f) photocurrent responsive profiles of **PyDBTSO-AA** and **PyDBTSO-AB** COFs. In (b), the photoluminescent spectra of **DBTSO-imine** and **Py-imine** compounds are displayed for comparison. (g and j) Pseudo colour images of femtosecond transient absorption spectra, (h and k) transient absorption spectra at different decay time, and (i and l) decay curves monitored at 480 nm of (g–i) **PyDBTSO-AA** and (j–l) **PyDBTSO-AB** COFs.

generation in the photocatalysis system. As shown in Fig. 3e, the first semicircle arc in the Nyquist plot of **PyDBTSO-AB** showed a much smaller radius than that of **PyDBTSO-AA**, illustrating that the charge transport in the former is much lower than that in the latter. Furthermore, as compared with the **PyDBTSO-AA** film, the **PyDBTSO-AB** film can respond to light illumination with a significantly enhanced photocurrent (Fig. 3f). This indicates that photo-produced excitons in the **PyDBTSO-AB** film can dissociate into free charge carriers much more efficiently than in the **PyDBTSO-AA** film, which would enable higher photocatalytic performance.

To gain insight into the exciton generation and dissociation processes, femtosecond transient absorption spectroscopy (fs-TAS) was conducted. As shown in Fig. 3g and h, when pumped with a 440 nm laser, **PyDBTSO-AA** exhibited positive transient light absorption from 450 nm to 575 nm, which is assignable to photoinduced excited state absorption (PIA). Meanwhile, the negative transient light absorption originating from the ground-state bleach (GSB) appeared in the range of 575–750 nm. In the case of **PyDBTSO-AB** (Fig. 3j and k), a similar PIA band was observed in the region of 460–500 nm, narrower than that of **PyDBTSO-AA**. To analyze the electron trapping

mechanism and photogenerated carrier kinetics, the decay profiles of transient absorption at 480 nm (Fig. 3i and l) were fitted with a bi-exponential function. As compared to **PyDBTSO-AA**, **PyDBTSO-AB** was found to have a shorter lifetime in the first component (**PyDBTSO-AA**: 31.54 ps, **PyDBTSO-AB**: 24.35 ps), but a longer lifetime in the second component (**PyDBTSO-AA**: 1.24 ps, **PyDBTSO-AA**: 473.26 ps). Since the first component corresponds to a shallow electron trapping process, the shorter lifetime means the process is beneficial for **PyDBTSO-AB**. While the second component originates from exciton dissociation into a free charge carrier, the longer lifetime means photogenerated excitons in **PyDBTSO-AB** remain alive for a longer time and the electron–hole recombination process is more strongly inhibited. All these factors enable **PyDBTSO-AB** COF to achieve better photocatalytic activity.

Finally, the two synthesized COFs were applied as photocatalysts for light-driven hydrogen production reactions, and their photocatalytic performances were compared. In a typical photocatalysis experiment, 1.5 mg of COF photocatalyst was dispersed in a reaction medium composed of 0.5 mL *N*,*N*-dimethylformamide (DMF), 15 mL deionized water, and 1.5 mmol ascorbic acid (AA). Here, DMF was used as a co-solvent to assist the dispersion of COF photocatalyst into water, while AA was used as a sacrificial electron donor. Subsequently, H_2PtCl_6 was added to the system to produce 1% Pt co-catalyst *via* photolysis. As shown in Fig. 4a, such systems can continuously produce hydrogen upon exposure to a 300 W Xe lamp with hydrogen evolution rates (HERs) of 38.4 mmol g^{-1} h^{-1} for **PyDBTSO-AA** and 83.4 mmol g^{-1} h^{-1} for **PyDBTSO-AB**. It was found that Pt loading has a significant effect on photocatalysis. In the absence of Pt co-catalyst, the activities of both **PyDBTSO-AA** and **PyDBTSO-AB** were very low (Fig. S6a and b†). After adding 1% Pt co-catalyst, the photocatalytic activities were dramatically enhanced. However, further increasing the Pt loading had the opposite effect, suggesting that 1% Pt loading was the optimal for both photocatalysis systems. Besides Pt loading, the photocatalyst dosage was found to influence HER; its value decreased with increasing

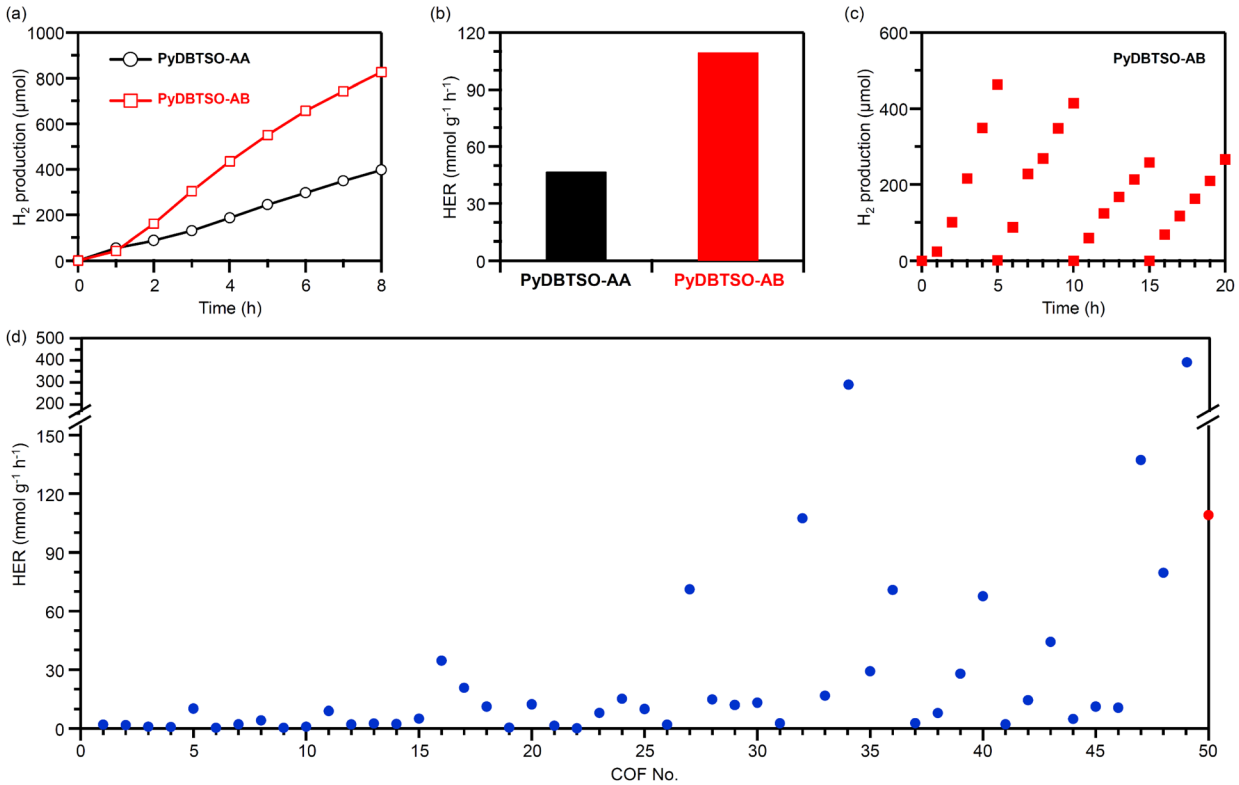

Fig. 4 (a) Time courses of photocatalytic hydrogen production using **PyDBTSO-AA** and **PyDBTSO-AB** as photocatalysts. Other conditions: 1.5 mg of photocatalyst, 1 wt% Pt, and full-arc Xe-light irradiation. (b) Optimized hydrogen evolution rates of **PyDBTSO-AA** and **PyDBTSO-AB** under full-arc Xe light irradiation. (c) Recycling and reusability of **PyDBTSO-AB** in photocatalytic hydrogen production. Other conditions: 5 mg of photocatalyst, 2 wt% Pt, and full-arc Xe light irradiation. (d) Comparison of hydrogen evolution rate among reported COF photocatalysts. COF No. (1) TFPT-COF;[24] (2) N3-COF;[57] (3) OB-POP-3;[58] (4) N2-COF;[59] (5) FS-COF;[25] (6) TP-BDDA;[60] (7) sp^2c-COFERDN;[61] (8) g-$C_{40}N_3$-COF;[62] (9) g-$C_{18}N_3$-COF;[63] (10) TPDTz COF;[64] (11) Py-CITP-BT-COF;[31] (12) PyTz-COF;[65] (13) g-$C_{54}N_6$-COF;[66] (14) COF-alkene;[67] (15) PyTA-BC;[68] (16) Tp-2C/BPy2+-COF;[69] (17) TtaTfa;[70] (18) PEG@BT-COF;[71] (19) ZnPor-DETH-COF;[72] (20) T-COF@CdS-3;[73] (21) BDF-TAPT-COF;[74] (22) TFA-COF;[75] (23) NKCOF-108;[76] (24) BTH-3;[26] (25) COF-OH-3;[77] (26) v-2D-COF-NO1;[78] (27) PY-DHBD-COF;[79] (28) TpPa-Cu-COF;[80] (29) TTAN-COF;[81] (30) NKCOF-113-M;[82] (31) ODA-COF;[83] (32) COF-JLU100;[30] (33) TAPT-TFPA;[84] (34) ZVCOF-1;[28] (35) TP-COF;[85] (36) TCDA-COF;[27] (37) TAPFy-PhI COF;[32] (38) TAPT-OMe-alkyne-COF;[33] (39) DCNA-1;[86] (40) COF-935;[87] (41) PyAl-TpbAm-COF;[88] (42) S2-TP COF;[89] (43) Py-hCOF;[90] (44) Macro TpBpy;[91] (45) ZnP-Tt;[92] (46) HKUST-1/TpPa-1;[93] (47) COF-954;[56] (48) Q1DCOF-13;[94] (49) COF/HOF heterojunction;[29] and (50) **PyDBTSO-AB** (this work).

photocatalyst dosage from 0.5–3.5 mg (Fig. S6c and d†). Under the optimized conditions, the HERs reached 46.8 mmol g^{-1} h^{-1} for **PyDBTSO-AA** and 109.6 mmol g^{-1} h^{-1} for **PyDBTSO-AB** (Fig. 4b); thus, the latter is more than twice that of the former. This clearly indicates that the change of interlayer stacking mode from eclipsed AA to staggered AB greatly improves the photocatalytic performance of the COFs. More importantly, of the COF photocatalysts reported to date, only a few COFs (COF-JUL100,[30] ZV-COF-1,[28] COF-954,[56] and COF/HOF hybrid[29]) delivered a HER higher than 100 mmol g^{-1} h^{-1} (Fig. 4d). Clearly, **PyDBTSO-AB** outperforms most reported COF photocatalysts. Even when the comparison is carried out among all-organic semiconductor photocatalysts (Table S2†), the HER of 109.6 mmol g^{-1} h^{-1} is an impressively high value. Moreover, the apparent quantum yields (AQYs) of **PyDBTSO-AB** at a dosage of 0.5 mg were measured to be 0.41% at 420 nm and 0.27% at 500 nm. In a four-round light on-off photocatalysis experiment, shown in Fig. 4c, the activity of **PyDBTSO-AB** was found to be similar in the first two rounds but decreased from the third round. Since a certain amount of photocatalyst was observed to stick to the upper glass wall during the reaction, it may be reasonable to observe such a decrement in the third round. In fact, XRD analyses before and after photocatalysis (Fig. S7†) found almost no change, confirming the robustness of the photocatalysts.

As aforementioned, AA-stacking generally helps a D–A COF achieve higher photocatalytic activity than AB-stacking. However, in this work, we observed the converse. After checking and identifying their structural differences and properties, we found only one factor that was beneficial for photocatalysis by **PyDBTSO-AA**. That is, **PyDBTSO-AA** has a much larger SSA and pore volume than **PyDBTSO-AB**. However, at least two aspects support the higher photocatalytic performance of **PyDBTSO-AB** over **PyDBTSO-AA**. (1) Hydrophilicity. In the water contact angle measurements shown in Fig. S8,† **PyDBTSO-AB** exhibited a smaller water contact angle than **PyDBTSO-AA** (127.17 *vs.* 145.06°), showing that the former is more hydrophilic than the latter. Moreover, it was difficult to disperse **PyDBTSO-AA** in water and in the photocatalysis medium containing AA. This is evidenced by the color change from bright yellow for a freshly prepared **PyDBTSO-AA** water dispersion to grayish yellow with some precipitates at the bottom after standing for a few hours or upon the addition of AA into the system (Fig. S9†). In contrast, such phenomena were not observed for **PyDBTSO-AB**. As suggested from the IR spectra shown in Fig. 1b, the edges of **PyDBTSO-AB** sheets are mostly furnished with primary amine units, whereas those of **PyDBTSO-AA** sheets possess aldehyde functional groups. Thus, it is reasonable to deduce that the different hydrophilicities arise from their different edge functionalities. (2) Interlayer packing distance. The AA-stacking of a D–A COF favors the formation of spatially segregated D and A one-dimensional columns. If the interlayer distance is sufficiently short, such columns can effectively establish additional charge transport pathways for both holes and electrons, besides their conjugated framework backbones. However, structural simulations suggest that **PyDBTSO-AA** crystals have an interlayer packing distance of 4.56 Å (Fig. 1d), implying that no intense π–π interactions exist among the sheets. Furthermore, the XRD pattern (Fig. 1d) did not show any peaks in the 2θ range of 20°–25°, confirming no regular packing along the interlayer stacking direction. Therefore, the AA-stacking mode in **PyDBTSO-AA** crystals does not seem to provide additional hole and electron charge transport pathways. However, in the case of **PyDBTSO-AB** crystals, structural simulations suggest the interlayer stacking through DBTSO units in the middle of linear arms with a distance of 3.90 Å (Fig. 1e), which can be calculated from the *c* parameter and the fact that two sheets appear in one crystalline cell. Moreover, its XRD pattern displayed a sharp peak at 2θ of 25.1°, corresponding to a *d*-spacing of 3.42 Å. These observations suggest intense π–π interactions among **PyDBTSO-AB** sheets *via* DBTSO units and an additional electron transport pathway in the crystals.

Furthermore, theoretical calculations were conducted to gain insight into the discrepancies of the band structure and electronic states triggered by the different interlayer packing structures. As shown in Fig. 5a, **PyDBTSO-AB** displays a larger density of states (DOS) in both CB and VB than **PyDBTSO-AA**. Clearly, as compared to **PyDBTSO-AA**, **PyDBTSO-AB** has a greater number of electrons ready to be photo-excited in its VB, and can accept more excited electrons in its CB. This illustrates that the change in the interlayer packing from AA to AB enables more charge separation to take place upon photoexcitation. Furthermore, the highest occupied molecular orbital (HOMO)s of both **PyDBTSO-AA** and **PyDBTSO-AB** are contributed mainly from Py moieties (Fig. 5b), while the lowest unoccupied molecular orbital (LUMO) of **PyDBTSO-AB** seems to be more localized in the DBTSO units and its neighbor phenylene linkers than that of **PyDBTSO-AA**. In the electrostatic potential (ESP) mappings shown in Fig. 5c, the positive potentials are widely distributed in Py and phenylene linkers, while the negative potentials are centered at the sulfone moieties in DBTSO and the imine units. More importantly, it is found that such charge separation is more pronounced in **PyDBTSO-AB** than in **PyDBTSO-AA**, suggesting that the change of layer stacking from AA to AB mode promotes electron transfer from Py to DBTSO units. These analyses and theoretical studies suggest significant differences in the charge separation and transportation between the two studied COFs. As illustrated in Fig. 5d, **PyDBTSO-AB** is proposed to have an efficient intralayer charge separation between Py and DBTSO moieties and an interlayer electron-transport pathway through the π-packing DBTSO column. Although **PyDBTSO-AA** seems to establish segregated Py and DBTSO columns for the transportation of electron and hole charge carriers, respectively, the large interlayer distance may make these two charge transportation pathways less effective. Thus, it is reasonable to observe the smaller charge transport impedance and the larger photocurrent response in the **PyDBTSO-AB** film rather than in the **PyDBTSO-AA** film. These factors ultimately contribute to a much higher photocatalytic activity for **PyDBTSO-AB** COF bearing a special AB-stacking mode.

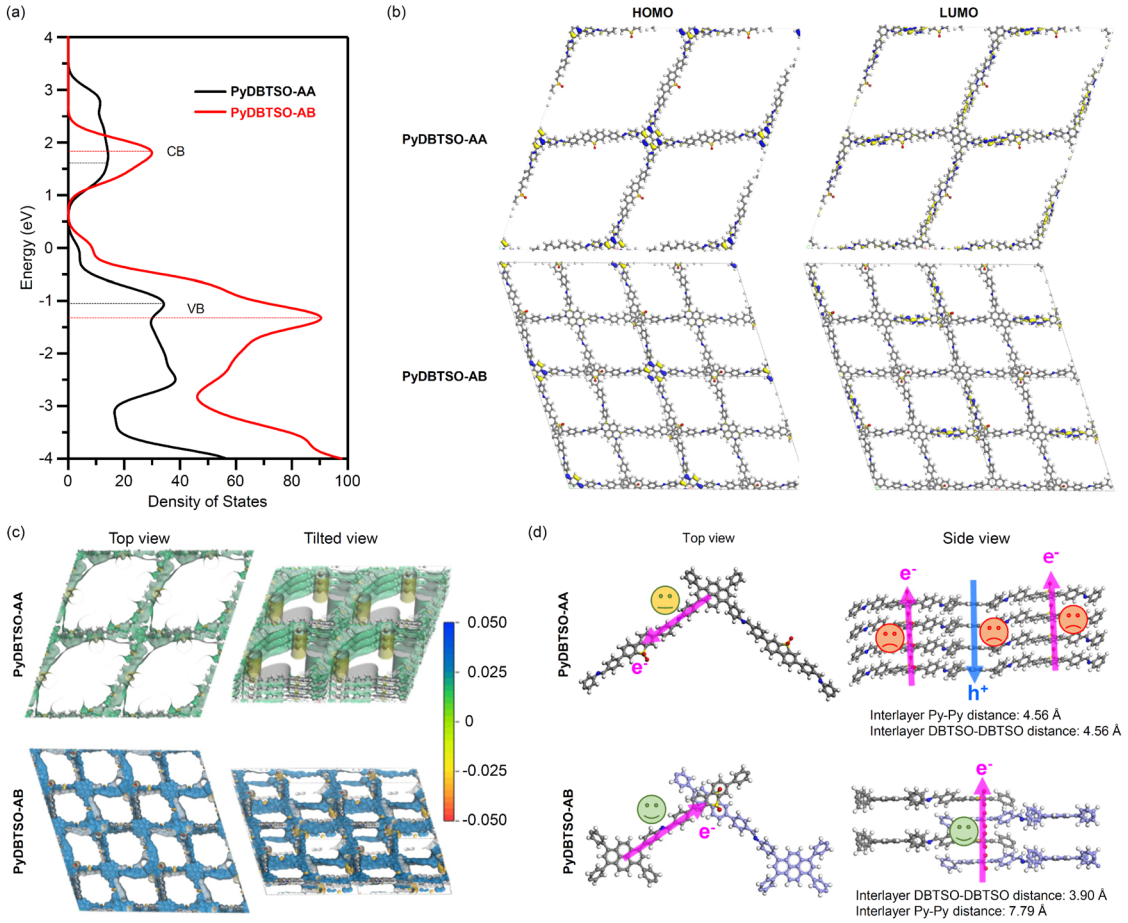

Fig. 5 (a) Density of states, (b) HOMO and LUMO (c) electrostatic potentials, and (d) representative illustrations of intralayer charge separation and interlayer charge transport pathways of PyDBTSO-AA and PyDBTSO-AB crystals.

Conclusions

In this work, a pair of iso-structured imine COFs, featuring the same D–A chemical scaffold but distinct interlayer stacking modes, were synthesized and their photocatalytic activities in light-driven hydrogen production reaction were compared. Utilizing the same tetraaniline-functionalized Py monomer and dibenzaldehyde-functionalized DBTSO monomer, imine polycondensation reactions were conducted under conventional solvothermal conditions in a mixture of oDCB and BuOH in the presence of AcOH as acid catalyst, resulting in the synthesis of **PyDBTSO-AA** COF with an AA-stacking mode. Conversely, when performed under ionothermal conditions in $[C_4mim][BF_4]$ ionic liquid, the same reactions produced **PyDBTSO-AB** COF with an AB-stacking mode. Comparative property analyses revealed that **PyDBTSO-AA** possesses a larger SSA and higher pore volume, whereas **PyDBTSO-AB** exhibits greater hydrophilicity. More significantly, the interlayer π–π stacking in **PyDBTSO-AB** crystals was found to be more intense than that in **PyDBTSO-AA** crystals. Due to these comprehensive effects, **PyDBTSO-AB** displayed reduced charge transport impedance and enhanced photo-current responsibility, ultimately resulting in superior photocatalytic performance. Accordingly, this research provides an atypical exemplar illustrating that AB-stacking COF can transcend the performance of AA-stacking COF, thereby highlighting the profound impact of interlayer stacking mode modulation on COF properties and photocatalytic activities.

Data availability

The data supporting this article have been included as part of the ESI.†

Author contributions

K.-H. L.: data curation, formal analysis, investigation, methodology, validation, and writing the original draft. L.-N. L., Z.-X. X., Z.-W. X., and Yogesh Gawale: investigation and methodology. F.-G. Z.: resources, supervision, writing – review and editing. W.-S. L.: conceptualization, formal analysis, funding acquisition, project administration, resources, supervision, validation, visualization, writing – review and editing.

Conflicts of interest

There are no conflicts to declare.

Acknowledgements

The authors gratefully acknowledge the Strategic Priority Research Program of the Chinese Academy of Science (No. XDB0590000), the National Natural Science Foundation of China (No. 52261145698), the Shanghai Institute of Organic Chemistry (No. sioczz202123), the Zhejiang Sci-Tech University Fundamental Research Fund (No. 23062110-Y), and the Zhengzhou University of Technology for financial support.

Notes and references

1 S. Berardi, S. Drouet, L. Francas, C. Gimbert-Surinach, M. Guttentag, C. Richmond, T. Stoll and A. Llobet, *Chem. Soc. Rev.*, 2014, **43**, 7501–7519.
2 M. Xia, X. Zhao, Y. Zhang, W. Pan and D. Y. C. Leung, *J. Mater. Chem. A*, 2022, **10**, 25380–25405.
3 J. Barber, *Chem. Soc. Rev.*, 2009, **38**, 185–196.
4 Z. Wang, C. Li and K. Domen, *Chem. Soc. Rev.*, 2019, **48**, 2109–2125.
5 M. Z. Rahman, F. Raziq, H. Zhang and J. Gascon, *Angew. Chem., Int. Ed.*, 2023, **62**, e202305385.
6 C. Dai and B. Liu, *Energy Environ. Sci.*, 2020, **13**, 24–52.
7 S. Cao, J. Low, J. Yu and M. Jaroniec, *Adv. Mater.*, 2015, **27**, 2150–2176.
8 S. Qiao, M. Di, J.-X. Jiang and B.-H. Han, *EnergyChem*, 2022, **4**, 100094.
9 J. M. Lee and A. I. Cooper, *Chem. Rev.*, 2020, **120**, 2171–2214.
10 V. S. Vyas, V. W.-h. Lau and B. V. Lotsch, *Chem. Mater.*, 2016, **28**, 5191–5204.
11 G. Zhang, Z. A. Lan and X. Wang, *Angew. Chem., Int. Ed.*, 2016, **55**, 15712–15727.
12 Z. Qian, Z. J. Wang and K. A. I. Zhang, *Chem. Mater.*, 2021, **33**, 1909–1926.
13 A. Iemhoff, M. Vennewald and R. Palkovits, *Angew. Chem., Int. Ed.*, 2023, **62**, e202212015.
14 C. Yang, B. Cheng, J. Xu, J. Yu and S. Cao, *EnergyChem*, 2024, **6**, 100116.
15 M. Z. Rahman, M. G. Kibria and C. B. Mullins, *Chem. Soc. Rev.*, 2020, **49**, 1887–1931.
16 T. He and Y. Zhao, *Angew. Chem., Int. Ed.*, 2023, **62**, e202303086.
17 J. Guo and D. Jiang, *ACS Cent. Sci.*, 2020, **6**, 869–879.
18 I. Ullah, M. Amin, P. Zhao, N. Qin and A.-W. Xu, *Inorg. Chem. Front.*, 2025, **12**, 1329–1348.
19 K. C. Christoforidis and P. Fornasiero, *ChemCatChem*, 2017, **9**, 1523–1544.
20 M. R. Shaner, H. A. Atwater, N. S. Lewis and E. W. McFarland, *Energy Environ. Sci.*, 2016, **9**, 2354–2371.
21 E. Jin, J. Li, K. Geng, Q. Jiang, H. Xu, Q. Xu and D. Jiang, *Nat. Commun.*, 2018, **9**, 4143.
22 S. Xu, H. Sun, M. Addicoat, B. P. Biswal, F. He, S. Park, S. Paasch, T. Zhang, W. Sheng, E. Brunner, Y. Hou, M. Richter and X. Feng, *Adv. Mater.*, 2021, **33**, e2006274.
23 M. G. Schwab, M. Hamburger, X. Feng, J. Shu, H. W. Spiess, X. Wang, M. Antonietti and K. Müllen, *Chem. Commun.*, 2010, **46**, 8932–8934.
24 L. Stegbauer, K. Schwinghammer and B. V. Lotsch, *Chem. Sci.*, 2014, **5**, 2789–2793.
25 X. Wang, L. Chen, S. Y. Chong, M. A. Little, Y. Wu, W.-H. Zhu, R. Clowes, Y. Yan, M. A. Zwijnenburg, R. S. Sprick and A. I. Cooper, *Nat. Chem.*, 2018, **10**, 1180–1189.
26 Y. Wang, W. Hao, H. Liu, R. Chen, Q. Pan, Z. Li and Y. Zhao, *Nat. Commun.*, 2022, **13**, 100.
27 Z. Li, T. Deng, S. Ma, Z. Zhang, G. Wu, J. Wang, Q. Li, H. Xia, S.-W. Yang and X. Liu, *J. Am. Chem. Soc.*, 2023, **145**, 8364–8374.
28 Z. Zhang and Y. Xu, *J. Am. Chem. Soc.*, 2023, **145**, 25222–25232.
29 R. Gao, R. Shen, C. Huang, K. Huang, G. Liang, P. Zhang and X. Li, *Angew. Chem., Int. Ed.*, 2025, **64**, e202414229.
30 S. Ma, T. Deng, Z. Li, Z. Zhang, J. Jia, G. Wu, H. Xia, S.-W. Yang and X. Liu, *Angew. Chem., Int. Ed.*, 2022, **61**, e202208919.
31 W. Chen, L. Wang, D. Mo, F. He, Z. Wen, X. Wu, H. Xu and L. Chen, *Angew. Chem., Int. Ed.*, 2020, **59**, 16902–16909.
32 G. Zhang, M. Zhao, L. Su, H. Yu, C. Wang, D. Sun and Y. Ding, *ACS Appl. Mater. Interfaces*, 2023, **15**, 20310–20316.
33 Y. Qian, Y. Han, X. Zhang, G. Yang, G. Zhang and H.-L. Jiang, *Nat. Commun.*, 2023, **14**, 3083.
34 Y. Wang, Z. Qiao, H. Li, R. Zhang, Z. Xiang, D. Cao and S. Wang, *Angew. Chem., Int. Ed.*, 2024, **63**, e202404726.
35 S. Ghosh, A. Nakada, M. A. Springer, T. Kawaguchi, K. Suzuki, H. Kaji, I. Baburin, A. Kuc, T. Heine, H. Suzuki, R. Abe and S. Seki, *J. Am. Chem. Soc.*, 2020, **142**, 9752–9762.
36 S. Yang, X. Li, Y. Qin, Y. Cheng, W. Fan, X. Lang, L. Zheng and Q. Cao, *ACS Appl. Mater. Interfaces*, 2021, **13**, 29471–29481.
37 P.-Y. You, K.-M. Mo, Y.-M. Wang, Q. Gao, X.-C. Lin, J.-T. Lin, M. Xie, R.-J. Wei, G.-H. Ning and D. Li, *Nat. Commun.*, 2024, **15**, 194.
38 Z. Gao, S. Lv, Y. Wang, Z. Xu, Y. Zong, Y. Tao, Y. Zhao, X. Liu, S. Yu, M. Luo, N. Khaorapapong, R. Zhang and Y. Yamauchi, *Adv. Sci.*, 2024, **11**, e2406530.
39 J.-l. Wang, G. Ouyang, D. Wang, J. Li, J. Yao, W.-S. Li and H. Li, *Macromolecules*, 2021, **54**, 2661–2666.
40 Z.-A. Lan, W. Ren, X. Chen, Y. Zhang and X. Wang, *Appl. Catal., B*, 2019, **245**, 596–603.
41 C. Shu, C. Han, X. Yang, C. Zhang, Y. Chen, S. Ren, F. Wang, F. Huang and J.-X. Jiang, *Adv. Mater.*, 2021, **33**, e2008498.
42 H. Zhao, Y. Dong, P. Sun, Y. Bai, C. Ru, X. Wu, Z. Li, X. Han, J. Wu and X. Pan, *ACS Appl. Energy Mater.*, 2022, **5**, 4631–4640.
43 C. Han, S. Xiang, S. Jin, L.-W. Luo, C. Zhang, C. Yan and J.-X. Jiang, *J. Mater. Chem. A*, 2022, **10**, 5255–5261.
44 Q. Li, J. Li, W.-R. Wang, L.-N. Liu, Z.-W. Xu, G. Xie, J. Li, J. Yao and W.-S. Li, *Chin. J. Chem.*, 2022, **40**, 2457–2467.
45 C. Cheng, X. Wang and F. Wang, *Appl. Surf. Sci.*, 2019, **495**, 143537.
46 M. Ran, X. Zhang, J. Lin, R. A. Borse, L. Zhang and Y. Wang, *J. Mater. Chem. A*, 2025, **13**, 1123–1134.

47 L. Zhang, Q.-G. Tan, S.-J. Xiao, G.-P. Yang, Q.-Q. Zheng, C. Sun, X.-L. Mao, J.-Q. Fan, R.-P. Liang and J.-D. Qiu, *Small*, 2023, **19**, e2207798.
48 W. Wang, H. Wang, X. Tang, J. Huo, Y. Su, C. Lu, Y. Zhang, H. Xu and C. Gu, *Chem. Sci.*, 2022, **13**, 8679–8685.
49 A. M. Putz, M. W. Terban, S. Bette, F. Haase, R. E. Dinnebier and B. V. Lotsch, *Chem. Sci.*, 2020, **11**, 12647–12654.
50 J. Zhao, Z. Qiao, Y. He, R. Zhang, H. Li, X. Song, D. Cao and S. Wang, *Angew. Chem., Int. Ed.*, 2024, **64**, e202414366.
51 P.-J. Tian, X.-H. Han, Q.-Y. Qi and X. Zhao, *Chem. Sci.*, 2024, **15**, 9669–9675.
52 J. Sun, H. Sekhar Jena, C. Krishnaraj, K. Singh Rawat, S. Abednatanzi, J. Chakraborty, A. Laemont, W. Liu, H. Chen, Y. Y. Liu, K. Leus, H. Vrielinck, V. Van Speybroeck and P. Van Der Voort, *Angew. Chem., Int. Ed.*, 2023, **62**, e202216719.
53 W. Wu, Z. Li, S. Liu, D. Zhang, B. Cai, Y. Liang, M. Wu, Y. Liao and X. Zhao, *Angew. Chem., Int. Ed.*, 2024, **63**, e202404563.
54 F. Auras, L. Ascherl, A. H. Hakimioun, J. T. Margraf, F. C. Hanusch, S. Reuter, D. Bessinger, M. Döblinger, C. Hettstedt, K. Karaghiosoff, S. Herbert, P. Knochel, T. Clark and T. Bein, *J. Am. Chem. Soc.*, 2016, **138**, 16703–16710.
55 D. Xu, B. Cheng, S. Cao and J. Yu, *Appl. Catal., B*, 2015, **164**, 380–388.
56 Y. Zhong, W. Dong, S. Ren and L. Li, *Adv. Mater.*, 2024, **36**, e2308251.
57 V. S. Vyas, F. Haase, L. Stegbauer, G. Savasci, F. Podjaski, C. Ochsenfeld and B. V. Lotsch, *Nat. Commun.*, 2015, **6**, 8508.
58 S. Bi, Z. A. Lan, S. Paasch, W. Zhang, Y. He, C. Zhang, F. Liu, D. Wu, X. Zhuang, E. Brunner, X. Wang and F. Zhang, *Adv. Funct. Mater.*, 2017, **27**, 1703146.
59 T. Banerjee, F. Haase, G. Savasci, K. Gottschling, C. Ochsenfeld and B. V. Lotsch, *J. Am. Chem. Soc.*, 2017, **139**, 16228–16234.
60 P. Pachfule, A. Acharjya, J. Roeser, T. Langenhahn, M. Schwarze, R. Schomacker, A. Thomas and J. Schmidt, *J. Am. Chem. Soc.*, 2018, **140**, 1423–1427.
61 E. Jin, Z. Lan, Q. Jiang, K. Geng, G. Li, X. Wang and D. Jiang, *Chem*, 2019, **5**, 1632–1647.
62 S. Bi, C. Yang, W. Zhang, J. Xu, L. Liu, D. Wu, X. Wang, Y. Han, Q. Liang and F. Zhang, *Nat. Commun.*, 2019, **10**, 2467.
63 S. Wei, F. Zhang, W. Zhang, P. Qiang, K. Yu, X. Fu, D. Wu, S. Bi and F. Zhang, *J. Am. Chem. Soc.*, 2019, **141**, 14272–14279.
64 B. P. Biswal, H. A. Vignolo-Gonzalez, T. Banerjee, L. Grunenberg, G. Savasci, K. Gottschling, J. Nuss, C. Ochsenfeld and B. V. Lotsch, *J. Am. Chem. Soc.*, 2019, **141**, 11082–11092.
65 W. Li, X. Huang, T. Zeng, Y. A. Liu, W. Hu, H. Yang, Y.-B. Zhang and K. Wen, *Angew. Chem., Int. Ed.*, 2021, **60**, 1869–1874.
66 J. Xu, C. Yang, S. Bi, W. Wang, Y. He, D. Wu, Q. Liang, X. Wang and F. Zhang, *Angew. Chem., Int. Ed.*, 2020, **59**, 23845–23853.
67 C. Mo, M. Yang, F. Sun, J. Jian, L. Zhong, Z. Fang, J. Feng and D. Yu, *Adv. Sci.*, 2020, **7**, 1902988.
68 A. F. M. El-Mahdy, A. M. Elewa, S.-W. Huang, H.-H. Chou and S.-W. Kuo, *Adv. Opt. Mater.*, 2020, **8**, 2000641.
69 Z. Mi, T. Zhou, W. Weng, J. Unruangsri, K. Hu, W. Yang, C. Wang, K. A. I. Zhang and J. Guo, *Angew. Chem., Int. Ed.*, 2021, **60**, 9642–9649.
70 J. Yang, A. Acharjya, M.-Y. Ye, J. Rabeah, S. Li, Z. Kochovski, S. Youk, J. Roeser, J. Gruneberg, C. Penschke, M. Schwarze, T. Wang, Y. Lu, R. van de Krol, M. Oschatz, R. Schomacker, P. Saalfrank and A. Thomas, *Angew. Chem., Int. Ed.*, 2021, **60**, 19797–19803.
71 T. Zhou, L. Wang, X. Huang, J. Unruangsri, H. Zhang, R. Wang, Q. Song, Q. Yang, W. Li, C. Wang, K. Takahashi, H. Xu and J. Guo, *Nat. Commun.*, 2021, **12**, 3934.
72 R. Chen, Y. Wang, Y. Ma, A. Mal, X.-Y. Gao, L. Gao, L. Qiao, X.-B. Li, L.-Z. Wu and C. Wang, *Nat. Commun.*, 2021, **12**, 1354.
73 Y. Wang, Z. Hu, W. Wang, H. He, L. Deng, Y. Zhang, J. Huang, N. Zhao, G. Yu and Y.-N. Liu, *Chem. Sci.*, 2021, **12**, 16065–16073.
74 G.-B. Wang, F.-C. Zhu, Q.-Q. Lin, J.-L. Kan, K.-H. Xie, S. Li, Y. Geng and Y.-B. Dong, *Chem. Commun.*, 2021, **57**, 4464–4467.
75 C. Liu, Y. Xiao, Q. Yang, Y. Wang, R. Lu, Y. Chen, C. Wang and H. Yan, *Appl. Surf. Sci.*, 2021, **537**, 148082.
76 Z. Zhao, Y. Zheng, C. Wang, S. Zhang, J. Song, Y. Li, S. Ma, P. Cheng, Z. Zhang and Y. Chen, *ACS Catal.*, 2021, **11**, 2098–2107.
77 Y. Chen, X. Luo, J. Zhang, L. Hu, T. Xu, W. Li, L. Chen, M. Shen, S.-B. Ren, D.-M. Han, G.-H. Ning and D. Li, *J. Mater. Chem. A*, 2022, **10**, 24620–24627.
78 S. Li, R. Ma, S. Xu, T. Zheng, G. Fu, Y. Wu, Z. Liao, Y. Kuang, Y. Hou, D. Wang, P. S. Petkov, K. Simeonova, X. Feng, L.-Z. Wu, X.-B. Li and T. Zhang, *J. Am. Chem. Soc.*, 2022, **144**, 13953–13960.
79 Y. Li, L. Yang, H. He, L. Sun, H. Wang, X. Fang, Y. Zhao, D. Zheng, Y. Qi, Z. Li and W. Deng, *Nat. Commun.*, 2022, **13**, 1355.
80 W. Weng and J. Guo, *Nat. Commun.*, 2022, **13**, 5768.
81 Y. Yang, N. Luo, S. Lin, H. Yao and Y. Cai, *ACS Catal.*, 2022, **12**, 10718–10726.
82 Z. Zhao, X. Chen, B. Li, S. Zhao, L. Niu, Z. Zhang and Y. Chen, *Adv. Sci.*, 2022, **9**, e2203832.
83 S. Yang, H. Lv, H. Zhong, D. Yuan, X. Wang and R. Wang, *Angew. Chem., Int. Ed.*, 2022, **61**, e202115655.
84 W. Zhao, P. Yan, H. Yang, M. Bahri, A. M. James, H. Chen, L. Liu, B. Li, Z. Pang, R. Clowes, N. D. Browning, J. W. Ward, Y. Wu and A. I. Cooper, *Nat. Synth.*, 2022, **1**, 87–95.
85 H. Liu, D. Wang, Z. Yu, Y. Chen, X. Li, R. Zhang, X. Chen, L. Wu, N. Ding, Y. Wang and Y. Zhao, *Sci. China Mater.*, 2023, **66**, 2283–2289.
86 J. Yang, S. Ghosh, J. Roeser, A. Acharjya, C. Penschke, Y. Tsutsui, J. Rabeah, T. Wang, S. Y. Djoko Tameu, M. Y. Ye, J. Gruneberg, S. Li, C. Li, R. Schomacker, R. Van

De Krol, S. Seki, P. Saalfrank and A. Thomas, *Nat. Commun.*, 2022, **13**, 6317.
87 K. Wang, Y. Zhong, W. Dong, Y. Xiao, S. Ren and L. Li, *Angew. Chem., Int. Ed.*, 2023, **62**, e202304611.
88 H. He, R. Shen, P. Zhang, G. Liang and X. Li, *J. Mater. Chem. A*, 2024, **12**, 227–232.
89 Z. Lin, S. Dai, S. Yao, Q.-C. Lin, M. Fu, L.-H. Chung, B. Han and J. He, *Chem. Sci.*, 2025, **16**, 1948–1956.
90 H. He, R. Shen, Y. Yan, D. Chen, Z. Liu, L. Hao, X. Zhang, P. Zhang and X. Li, *Chem. Sci.*, 2024, **15**, 20002–20012.
91 I. Khalil, P. Das, H. Kucukkececi, V. Dippold, J. Rabeah, W. Tahir, J. Roeser, J. Schmidt and A. Thomas, *Chem. Mater.*, 2024, **36**, 8330–8337.
92 L. Zou, D. Si, S. Yang, Z. Chen, Y. Huang and R. Cao, *Angew. Chem., Int. Ed.*, 2025, **64**, e202418319.
93 T. Ma, Z. Liu, J. Deng, E. Han, J. Liang and R. Wang, *ChemSusChem*, 2024, **17**, e202400987.
94 C. Yang, J. Le, Y. Kuang, Z. Meng, H. Dai, Y. Zhou and H. Qiu, *J. Am. Chem. Soc.*, 2024, **146**, 26198–26206.

